energies

MDPI

Article

End-of-Life Electric Vehicle Battery Deep-Discharge Device Using Current Recirculation and Single-Phase Grid-Tied Inverter

Elias Wooten, Naser Vosoughi Kurdkandi and Chris Mi *

Department of Electrical and Computer Engineering, San Diego State University, San Diego, CA 92182, USA; ewooten5176@sdsu.edu (E.W.); nvosoughikurdkandi@sdsu.edu (N.V.K.)
* Correspondence: cmi@sdsu.edu

Abstract

It is projected that, by 2030, the global stock of electric vehicles (EVs) will reach approximately 85 million units. When the capacity of EV batteries declines to 70–80% of their original performance, replacement becomes necessary, as the remaining capacity is inadequate to meet the operational requirements of automotive applications. Upon removal, these batteries retain significant material value and thus require proper recycling. However, their stored energy presents substantial safety risks, necessitating a controlled discharge process to mitigate potential hazards. This study presents the design and implementation of a system that integrates a boost converter with a single-phase grid-tied inverter to facilitate the safe transfer of energy from end-of-life (EoL) EV batteries to the electrical grid. The system was simulated in PLECS using a lithium-ion battery model and a non-ideal grid. The analysis shows that the system is stable and effective at transferring energy from the battery to the grid and heating the battery at the end of the process. This study identifies circuit operating conditions and control schemes that can enable the rapid, practical, and safe discharge of EV batteries without significant voltage relaxation.

Keywords: EV battery recycling; EoL batteries; deep discharge; current recirculation heating; boost converter; grid-tied inverter; energy recovery; battery safety

1. Introduction

Electric vehicle (EV) sales have scaled exponentially in recent years, spurring interest in what will happen to batteries at the end of their useful life in their original EV application [1]. The batteries have a typical lifespan of between 8 and 15 years, which means that sometime between 2030 and 2035 there will be at least a million EoL EV batteries needing to be processed [2].

From our market research, conducted through NSF's I-Corps, we found that these batteries are typically removed by their respective dealership's repair center, before being shipped back to the automotive company for refurbishing or remanufacturing evaluation. If they are not suited for this application, batteries are typically sold or bought by a third-party company to be evaluated for second-life storage. If they also fail this test, they are recycled, typically through one of three main recycling techniques [3,4].

One of the most popular recycling techniques used today is pyrometallurgy, employed by Redwood Materials, which captures around 70% of the EV battery recycling market in North America [3]. This process involves heating whole battery packs or segments of battery packs to between 650 and 1500 °C in a controlled environment, which burns off plastics and melts most of the metals down [3,5]. Pyrometallurgy requires less pack

Academic Editor: José Matas

Received: 16 February 2026
Revised: 4 May 2026
Accepted: 5 May 2026
Published: 9 May 2026

disassembly; however, this process results in the loss of other valuable battery components such as electrolytes, graphite, steel, aluminum, and lithium, which are either converted into slag or released as off-gases [6]. Moreover, pyrometallurgical processing requires costly gas effluent treatment systems to prevent the emission of toxic compounds into the atmosphere. In addition, this method offers no economic advantage when applied to low-value lithium-ion battery chemistries (e.g., $LiFePO_4$, $LiMnO_2$, or $LiTiO_4$), as their constituent elements are ultimately lost to the slag phase [7].

The second common recycling technique is hydrometallurgy, which employs liquids to process and sort the materials found in EV batteries [8]. The key advantages of hydrometallurgical recycling over pyrometallurgy are the recovery of high-purity metals, such as Ni, Co, Mn, Li, with greater than 99 percent recovery, as well as low impurity content [8,9].

Li-Cycle, a leading EV battery recycling company in North America, has adopted a variant of this method in which spent EV batteries are submerged in a liquid medium during shredding to suppress ignition and dissipate the heat generated throughout the process [6]. This approach offers advantages and limitations comparable to those of pyrometallurgical recycling. Notably, it eliminates the need for battery pack disassembly, enables the processing of severely damaged batteries, and accommodates a wide range of cell geometries without specialized tooling [10].

Other processes such as low-temperature plasma-assisted separation or traditional battery shredding require that the EoL battery be deeply discharged to below 5% state of charge (SoC) to avoid fires, improve material recovery percentage, and improve material recovery quality [11]. Current techniques to deep discharge the battery involve either a brine bath, a resistive load, or a grid-tied system without battery management system (BMS) integration.

Brine baths typically last over 100 h and release toxic gases that need to be vented, and, with certain types of battery casings, significant degradation to the case and cell materials will occur [12]. This degradation can cause certain hydrometallurgy techniques to be ineffective and can degrade the structure to the point where the pack can crumble and be unsafe to lift [12]. Brine baths essentially act as a fixed-resistance load at the battery terminals, which cannot be modulated per pack voltage [12]. High-power resistive loads for battery deep discharge have not been widely studied. However, they have key advantages over brine baths, such as the ability to modulate pack power by switching on and off the resistive load with a PWM transistor. Thus, this enables the resistance to be decreased as pack voltage decreases, which allows for shorter discharge times. However, resistive loads also have key disadvantages compared with grid-tied systems, including heat generation, system size, fan noise, and loss of the energy stored in the batteries.

Existing grid-tied set ups on the market require the partial disassembly of EV batteries so that their BMS can tap into every cell voltage and some key temperature points [13]. This is non-ideal because it exposes the technician to high voltage and has the potential for equipment to be hooked up incorrectly. It also drastically slows down the discharge process to allow for the battery to be disassembled and the sensors to be attached. This disassembly and rigging can take upwards of 8 h for some battery packs, and most battery packs would need specialized harnesses to tap into the existing voltage sense cabling. In some batteries, the voltage sensing would not be feasible to perform safely without module-level deconstruction, which would take up to another 8 h.

This paper suggests a novel alternative to existing deep-discharge techniques which address some of their key shortcomings through a novel application of a voltage relaxation technique and a novel current recirculation technique and control strategy. Specifically, a novel, power electronics based deep-discharge device is presented that offers a controllable and non-destructive method for rapidly reducing an EV battery's SoC to below

5% with minimal subsequent voltage relaxation. The proposed system integrates a boost converter, which also functions as a novel current recirculation circuit, in conjunction with a single-phase inverter, to facilitate controlled energy transfer from EoL EV batteries to the electrical grid.

The combined inverter and boost converter configuration enables compatibility with a wide range of EV battery architectures. Some key EV battery parameters that drive design decisions are internal resistance, thermal mass, and C rate. The upper limit of current recirculation capabilities is aimed at being able to heat the largest battery packs with the lowest internal resistance, the highest C-rate, and the greatest thermal mass. If the current recirculation capability is too low, then the system would not be able to effectively heat the batteries at the end of the discharge process. Section 4.3 discusses this in more detail.

During the final phase of the discharge process, the current recirculation circuit elevates the battery temperature to above 40 °C, significantly mitigating the risk of voltage relaxation [14]. Additionally, the compact and portable design of the device supports ease of operation in workshop environments, while the proposed control interface ensures intuitive user interaction.

The remainder of this paper is organized as follows. In Section 2, the design considerations are introduced along with the proposed circuit topology and operational modes. Section 3 discusses the design guidelines and controls of the system. In Section 4, the simulation results are demonstrated. Conclusions are drawn in Section 5.

2. Proposed System

The proposed system is designed for use by technicians in automotive service centers, recycling facilities that conduct in-house discharging operations, and automotive manufacturers performing battery evaluations. Consequently, several considerations must be addressed to ensure the device is practical and effective for the intended user base. These considerations are as follows:

1. The device should operate using a standard 50 A welder outlet (NEMA 14–50R).
2. Given the outlet constraints, the device must discharge the battery as quickly as possible.
3. Safety must be ensured at all stages of discharge.
4. The device must ensure <1 V per cell voltage relaxation.
5. EV battery packs of all sizes and configurations must be able to be processed.

To connect these qualitative design considerations to an implementable system architecture, each requirement was translated into a small set of quantitative, verifiable specifications. In particular, the outlet constraint (NEMA 14-50R) directly bounds the allowable grid voltage, frequency, and maximum grid current, which in turn limits the maximum continuous power that can be transferred from the battery to the grid. The discharge rate and safety requirements then motivate upper bounds on battery side and internal recirculating currents to ensure thermal and electrical stresses remain within acceptable limits while still enabling rapid energy removal. Finally, the requirements for broad pack compatibility and limited voltage relaxation establish the allowable EV pack voltage range and the current capability needed to reliably drive the pack below the specified residual energy threshold across diverse configurations. The resulting high-level specifications, which explicitly map back to the corresponding considerations, are summarized in Table 1.

Table 1. High-level specifications of the deep-discharge device.

Parameter	Value	Corrisponding Consideration
EV battery voltage	0–1000 V_{DC}	3, 5
Grid voltage	208–240 V_{AC}	1, 3
Grid frequency	60 Hz	1
Battery to grid power	11 kW	1, 2, 3
Max battery current	200 A	2, 3, 4, 5
Max grid current	50 A_{rms}	1, 3
Max recirculating battery current	200 A_{rms}	2, 3, 4, 5

It is worth noting that the device must be able to read the cell temperatures from the batteries' onboard battery management system (BMS). In a practical implementation of this design, the system would have a BMS gateway integrated into the device driver layer of the software and have the necessary hardware to support communication [15]. The temperatures of all the cells would need to be monitored approximately once per second to ensure that unexpected thermal behavior is caught and the device can be shut down, or in the case of Heating Mode, the outer control loop can toggle current recirculation. This integration is outside the scope of this paper and is therefore not discussed further.

2.1. Proposed Circuit Topology

The proposed circuit topology is shown in Figure 1. The system consists of a synchronous boost converter, which also functions as a current-recirculation heating circuit, connected to the EoL battery. The converter feeds a direct-current (DC) bus capacitor bank, which in turn supplies an H-bridge pulse-width modulation (PWM) inverter that interfaces with the grid through a 208–240 V single-phase connection. A neutral tap is incorporated to enhance operational safety. The general topology is inspired by the work in Dr. Hart's power electronics book [16]. In the simulation model, the grid and EoL battery are represented by lumped impedance elements, with the associated inductance and resistance parameterized in L_1, L_2, L_3, and the center-tap branch. This is because the line inductance and impedances will be much lower than the lumped model values. Measurement noise is neglected to reduce model complexity and to improve computational efficiency during simulation runs.

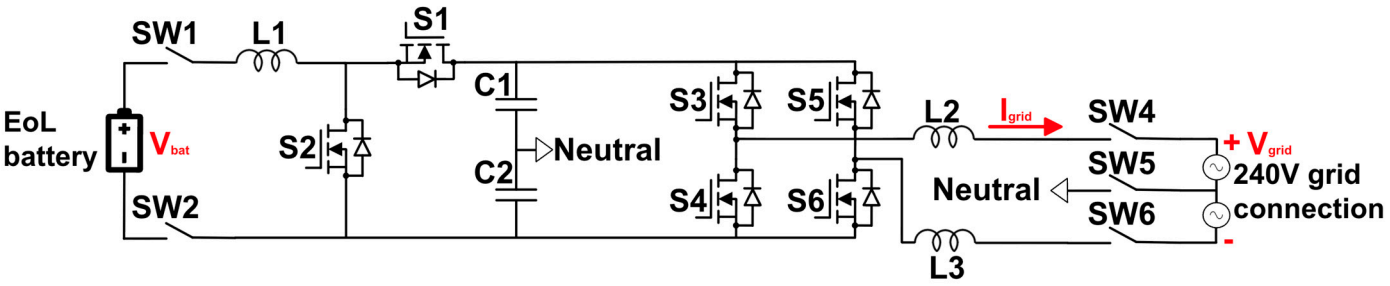

Figure 1. System topology. A synchronous boost stage (also used for current-recirculation heating) interfaces the EoL battery with a DC bus (C1–C2) that feeds a single-phase H-bridge inverter tied to a 208–240 V grid. A neutral tap is included for safety.

2.2. Operational Modes of the Proposed System

The proposed system operates in four distinct modes: (1) Bypass Mode, in which the inverter is directly connected to the EoL battery; (2) Boost Mode, where the boost converter is engaged between the inverter and the EoL battery to elevate the DC-bus voltage above the grid's peak voltage; (3) Heating Mode, which circulates current into and out of the EoL battery to raise its temperature above 40 °C; and (4) Short-Circuit Mode, wherein the EoL

battery is directly shorted to extract the remaining energy when the terminal voltage is sufficiently low. Each operating mode is characterized by its own distinct state transitions. The overall operational flow between these four modes is illustrated in Figure 2.

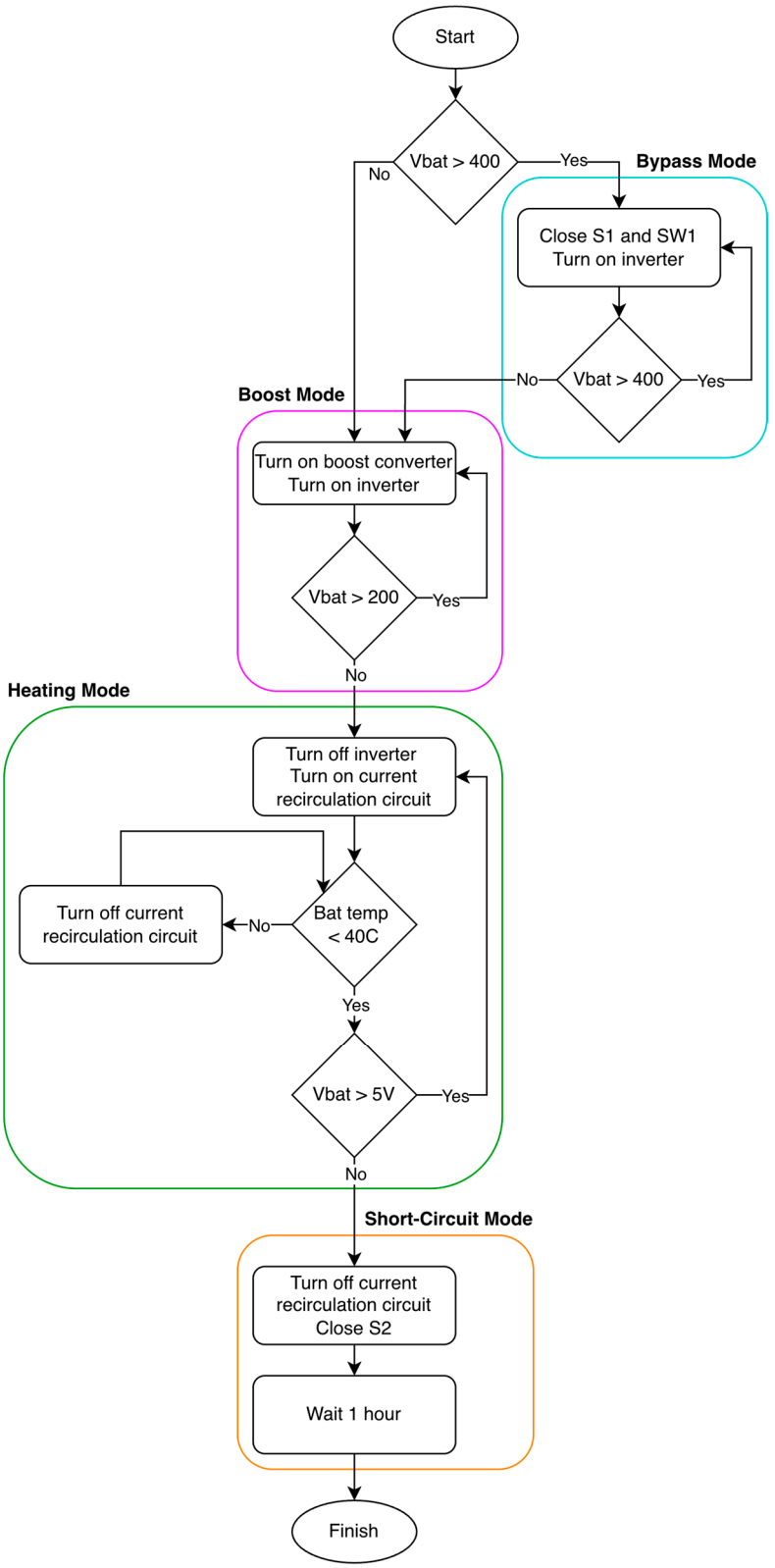

Figure 2. Whole-system state machine.

2.3. Bypass Mode

Bypass Mode: When $V_{bat} \geq 400$ V, the inverter draws directly from the pack (S1 on), avoiding DC-bus overshoot.

Bypass Mode mitigates voltage overshoot by allowing Boost Mode to activate at a lower EoL battery voltage. In this mode, switch S1 and the inverter are engaged, enabling the inverter to draw energy directly from the EoL battery. Bypass Mode is utilized only when the EoL battery voltage exceeds 400 V, as operation below this threshold prevents the inverter from achieving a peak voltage greater than that of the grid.

Within Bypass Mode, four distinct operating states arise due to the interaction between the inverter's PWM and the single-phase grid characteristics. In the first state, illustrated in Figure 3a, both S3 and S6 are active, and current is drawn from both the EoL battery and capacitors C1 and C2. Figure 3b depicts the system behavior during the positive half cycle, when S3 and S6 are deactivated for the complementary PWM interval, causing current to flow through the body diodes of S4 and S5. It is important to note that during this state, the EoL battery continues to experience a positive current draw even after the switching transition, owing to the stored energy in inductor L1. The third state, shown in Figure 3c, occurs during the grid's negative half cycle, when S4 and S5 are active, maintaining a positive current draw from the EoL battery and slightly discharging C1 and C2. In the final state, S4 and S5 are turned off, and current is redirected through the body diodes of S3 and S6, replenishing the charge on C1 and C2.

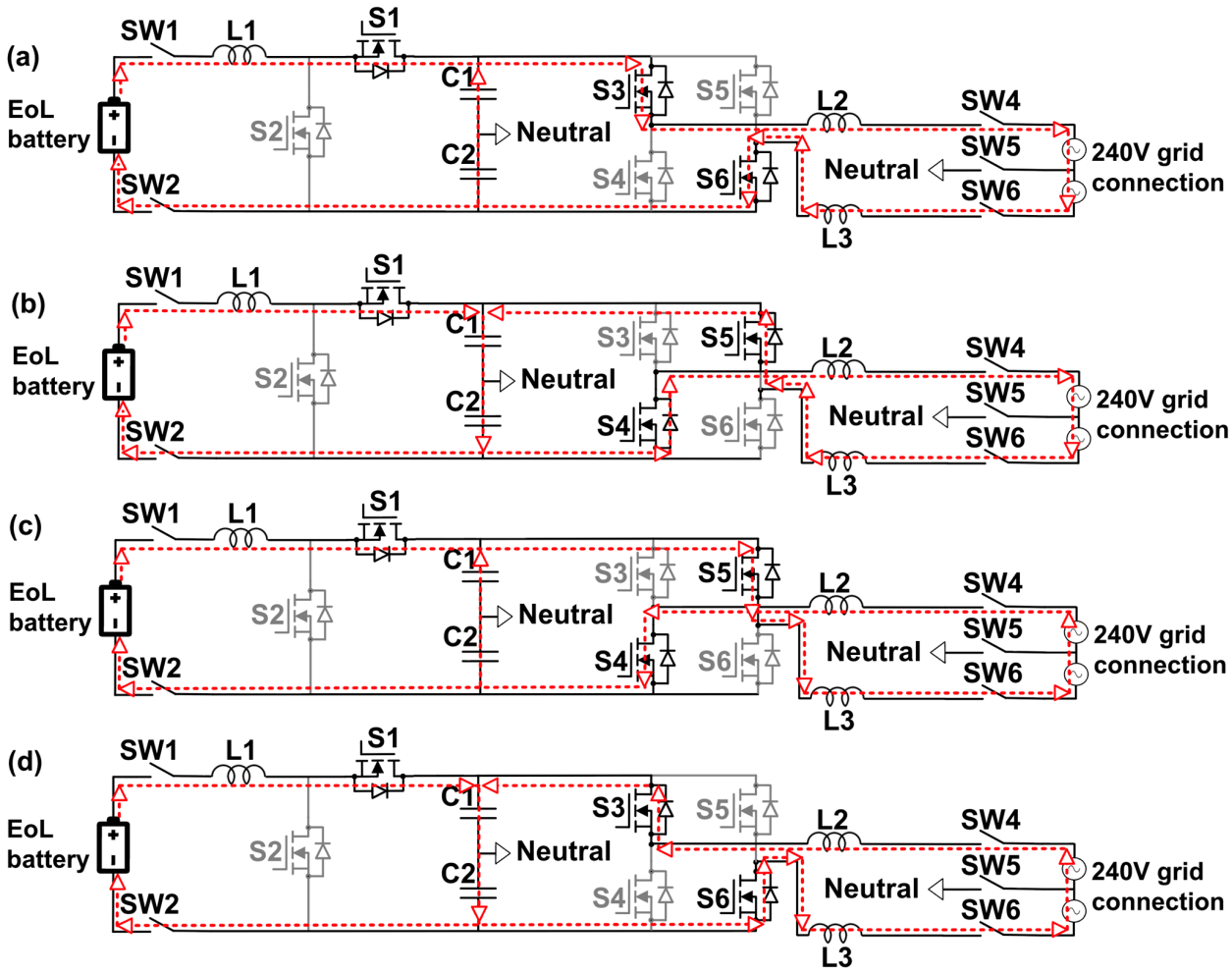

Figure 3. (**a**) Bypass Mode in positive half cycle with S3 and S6 active; (**b**) Bypass Mode in positive half cycle with S4 and S5 active; (**c**) Bypass Mode in negative half cycle with S4 and S5 active; (**d**) Bypass Mode in negative half cycle with S3 and S6 active.

2.4. Boost Mode

Boost Mode: When V_{bat} < 400 V, the boost stage raises the DC bus above grid peak, so the inverter remains grid-synchronized.

During Boost Mode, S2 periodically shorts the EoL battery through L1, storing energy in its magnetic field during the energy storage state. When S2 turns off, the stored energy is released through the body diode of S1 into the DC-bus capacitors C1 and C2, thereby elevating the DC-bus voltage above the battery voltage. This process allows the inverter to maintain grid-synchronized operation even when the EoL battery voltage is below the grid's peak value.

Boost Mode has eight total operating states and shares four with Bypass Mode as shown in Figure 3 and explained in Section 2.3. The other four operating states are shown in Figure 4 and consist of the same four inverter states but with the boost converter section in the energy storage state rather than bypass state.

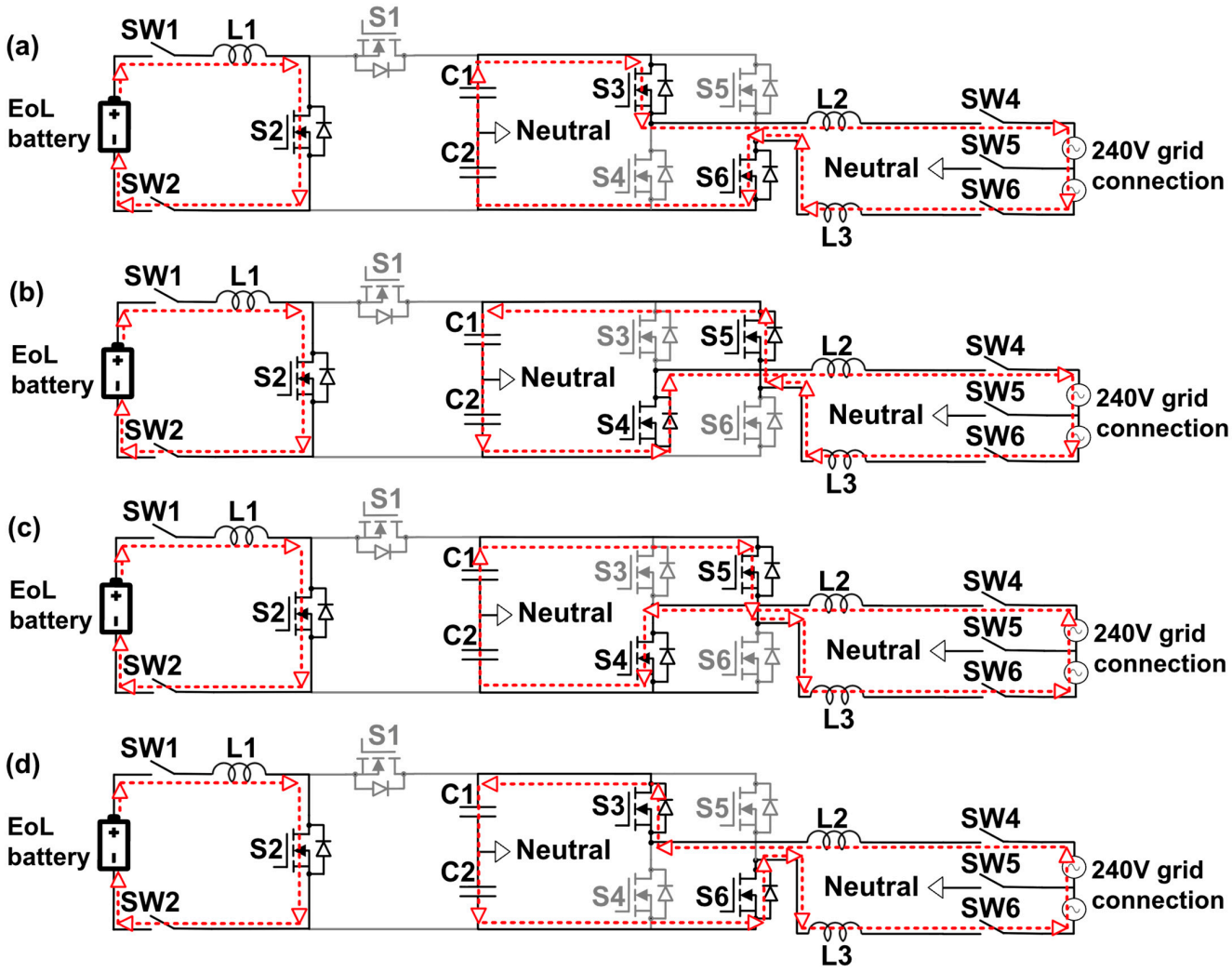

Figure 4. (**a**) Boost Mode in energy-storage state with S3 and S6 active in the positive half cycle; (**b**) Boost Mode in energy-storage state with S4 and S5 active in the positive half cycle; (**c**) Boost Mode in energy-storage state with S4 and S5 active in the negative half cycle; (**d**) Boost Mode in energy-storage state with S3 and S6 active in the negative half cycle.

2.5. Heating Mode

Heating Mode: Below 200 V, the boost hardware recirculates current into/out of the pack to raise temperature above 40 °C and extract residual energy. Figure 5 shows this current flow.

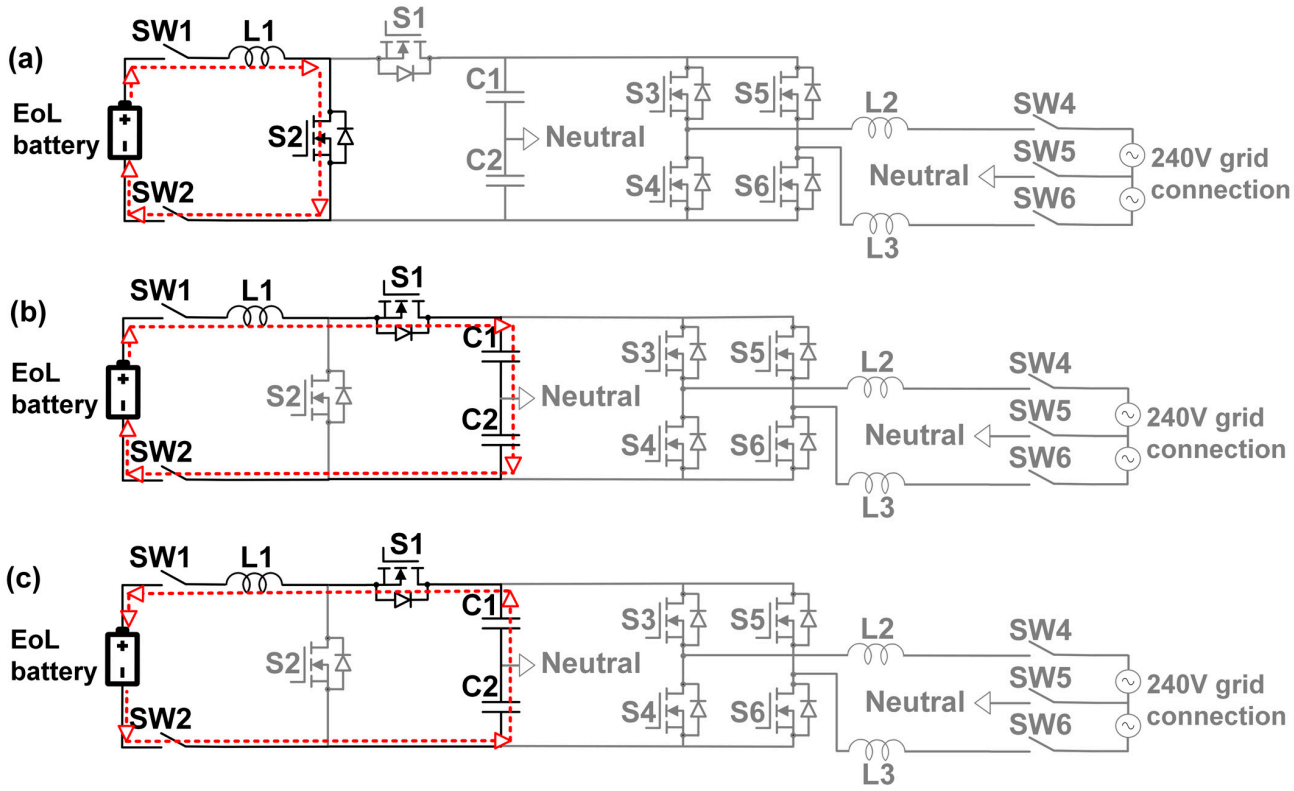

Figure 5. (**a**) Heating Mode in energy-storage cycle; (**b**) Heating Mode in active cycle; (**c**) Heating Mode in feedback cycle.

Heating Mode circulates current into and out of the EoL battery to elevate its temperature above 40 °C while extracting additional residual energy. The elevated temperature helps mitigate excessive post-discharge voltage relaxation [14]. This mode operates by initially shorting the EoL battery to ground through switch S2, allowing inductor L1 to store energy that is subsequently transferred to capacitors C1 and C2 via switch S1. Once the energy in L1 is fully discharged into the capacitors, the current through S1 reverses direction, causing the stored energy in C1 and C2 to be transferred back into the EoL battery. Heating Mode is engaged once Boost Mode becomes ineffective below around 200 V and remains active until the system transitions to Short-Circuit Mode at approximately 5 V. Note that the 200 V threshold will be elaborated on in Section 3 of this paper and depends on the stability of the DC-bus voltage at lower EoL battery voltages.

2.6. Short-Circuit Mode

Short-Circuit Mode: Below 5 V, the pack is shorted through S2 and L1 under a current limit to remove remaining charge and suppress rebound. Figure 6 shows the current flow.

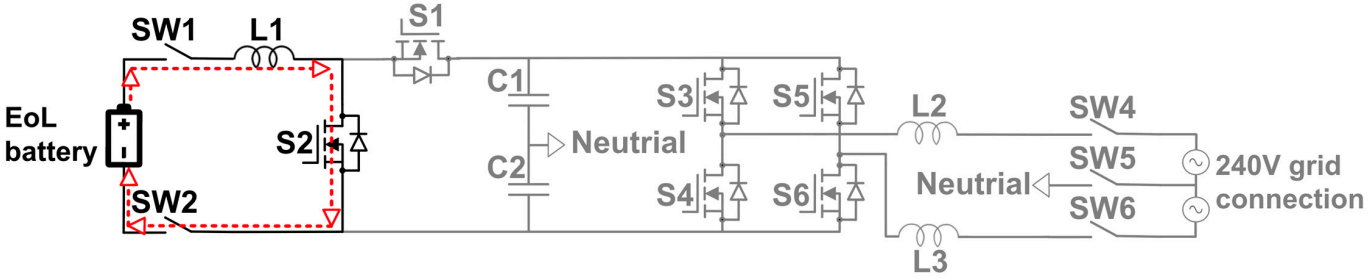

Figure 6. Short-Circuit Mode.

Short-Circuit Mode enables the final stage of the discharge process by allowing current to flow directly through the EoL battery. In this mode, switch S2 is activated, permitting a constant current to pass from the battery through S2 and inductor L1. This operating mode is initiated once the EoL battery voltage drops below 5 V and remains active for one hour to ensure complete energy removal and to mitigate excessive post-discharge voltage relaxation [17].

3. Design Guidelines and Control

This section outlines the methodology employed for sizing inductors L1–L3, capacitors C1–C2, and switches S1–S6, along with the derivation of duty cycle calculations across the various operating modes. It further elaborates on the rationale underlying the voltage thresholds that delineate these modes and describes the corresponding control strategies implemented for each.

3.1. Bypass Mode

As stated in Section 2.3, in Bypass Mode, S1 is always on and the inverter is active, to transfer energy from the EoL battery to the grid. As such, the primary mechanism of this mode is the PWM single-phase inverter, whose control and component sizing will be discussed in this section.

The fundamental control architecture of the PWM grid-tied inverter analyzed in this study is illustrated in Figure 7. The system operates under a current-controlled framework that employs a phase-locked loop (PLL) to generate a unit-amplitude cosine reference signal (1 V peak). This signal is multiplied by the current command, which is scaled by $\sqrt{2}$ to produce the root-mean-squared (RMS) current reference. The instantaneous current error is then obtained by subtracting the measured grid current from this reference. This error signal is processed by a proportional-resonant (PR) controller, the output of which is subsequently compared with a high-frequency sawtooth carrier waveform. When the PR controller output exceeds the sawtooth waveform, switches S4 and S5 are activated; conversely, when it falls below the sawtooth waveform, switches S3 and S6 are engaged. The overall system configuration and sawtooth-to-PWM control was informed by the methodology presented in [18].

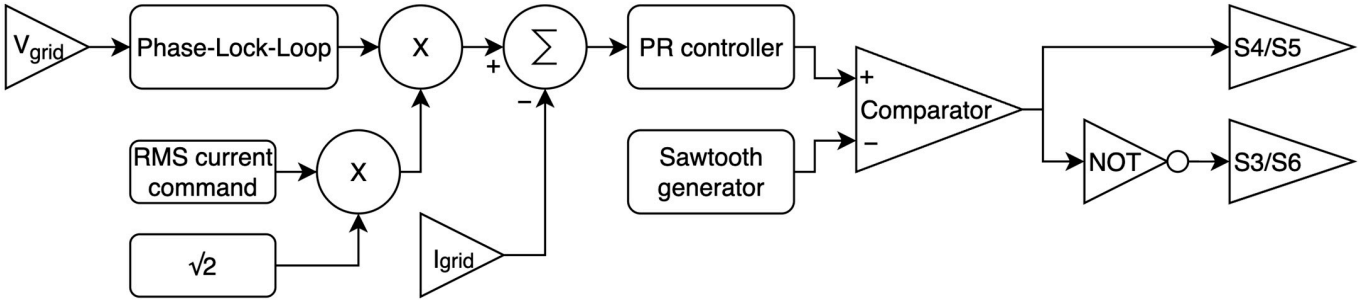

Figure 7. Block diagram of inverter controls.

To determine the appropriate component values, the desired grid current of 50 A, grid frequency of 60 Hz, and grid voltage range of 208–240 V_{AC}, as summarized in Table 1, were considered. A switching frequency of 50 kHz was selected, and the total inductance required was calculated using Equation (1) [18]. The resulting inductance was then equally divided between inductors L_2 and L_3.

$$L_{total} = \frac{V_{dcMax}}{4F_{sw}\Delta I_{ppMax}} \quad (1)$$

$$L_{total} = \frac{1000}{4(50,000)\left(\sqrt{2} \times 50\right)\left(2.5\sqrt{2}\right)} = 2 \text{ mH}, \quad (2)$$

This means that L2 = L3 = 1 mH. Similarly, for switches S_3–S_6, the maximum current rating is determined based on the peak grid current, calculated as $50 * \sqrt{2}$, and the continuous current rating would be half of the 50 A_{rms} rating because each of the four switches is only on for half of a whole grid cycle. The maximum voltage rating corresponds to the highest allowable DC-bus voltage of 1000 V. For a manufactured device, a factor of safety should be multiplied by these numbers to ensure safety.

The PR controller used is defined by Equation (3) [19], where the resonant angular frequency is given by $W_r = 2\pi 60 \frac{\text{rad}}{\text{sec}}$, the damping ratio is chosen as $\zeta = 0.01$, the integral gain is $K_i = 1$, and the proportional gain is $K_p = 0.02$. The parameters ζ and K_p were tuned by sweeping their values and selecting the combination that minimized the total harmonic distortion (THD) of the grid current.

$$G(s) = K_p + \frac{2K_i\zeta W_r s}{s^2 + 2\zeta W_r s + W_r^2} \quad (3)$$

Bypass Mode is employed when the EoL battery voltage lies between 400 V and 1000 V. Within this range, the DC-bus voltage is maintained above the peak grid voltage, $V_{gridPK} = 240\sqrt{2} \approx 339$ V, thereby preserving inverter stability and avoiding system faults. The lower bound of 400 V provides a safety margin that accounts for DC-bus ripple and the finite response time of the controller as the EoL battery voltage approaches this threshold. When the EoL battery voltage drops below 400 V, the inverter is disabled for 10 ms to allow the current to settle before the boost converter and inverter are re-enabled, at which point the system transitions into Boost Mode.

3.2. Boost Mode

Boost Mode operates similarly to Bypass Mode but with the boost stage active. Boost Mode defines DC-bus capacitance (represented by C1 and C2) as if the DC-bus voltage is too low; then, the ripple voltage can sag below the grid's peak voltage of ~339 V, which will cause the system to destabilize. Therefore, either C1 and C2 can be increased, or the DC-bus voltage can be boosted higher to allow for more voltage ripple. In this study, C1 and C2 are chosen to be 400 µF, and to avoid the poor performance of boost converters at very-low-duty ratios, the DC-bus voltage reference is set to 450 V. The duty ratio of the boost stage is determined by the ratio of the input and output voltages, as expressed in Equation (4) [20]. Rearranging Equation (4) yields the duty-cycle expression in Equation (5).

$$\frac{V_{out}}{V_{in}} = \frac{1}{1 - D} \quad (4)$$

$$D = 1 - \frac{V_{in}}{V_{out}} \quad (5)$$

Open-loop control is adopted for the boost stage because the dominant line-frequency harmonic at 120 Hz, arising from the single-phase inverter, is impractical to suppress via feedback control. An anti-windup scheme is also implemented to mitigate overshoot during start-up. Figure 8 illustrates how Equation (5) is implemented to accommodate variations in the EoL battery voltage.

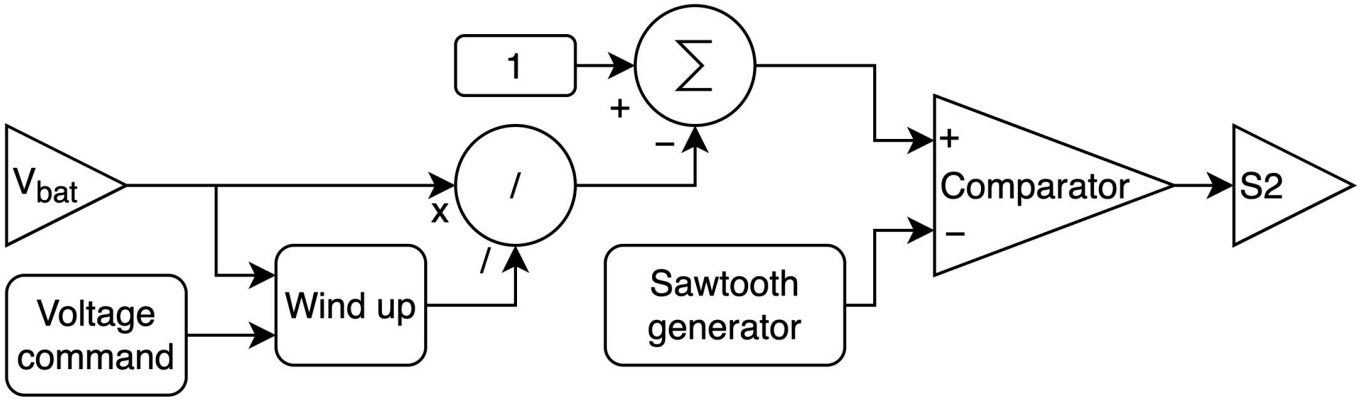

Figure 8. Block diagram of boost converter controls.

3.3. Heating Mode

Heating Mode disables the inverter and instead circulates current into and out of the EoL battery using only the boost-stage circuitry. The control architecture consists of a simple open-loop scheme that accepts an RMS current command and references the instantaneous EoL battery voltage to generate an inverted resistance command. This command is then multiplied by an equivalent resistance constant, R_{eq}, yielding a unitless scaling factor. The constant R_{eq} is defined as the ratio of the maximum EoL battery voltage to the maximum current that the system can deliver at that voltage when operating at a duty cycle of 0.1. To ensure that even a large battery can be heated and to increase the amount of power Heating Mode can dissipate from the battery, the desired circulating current is 150 A_{rms}. Because the duty cycle can be swept from 1 all the way down to 0.1, both S1 and S2 should be rated for the full 150 A_{rms} and the peak current defined by the RMS value multiplied by $\sqrt{3}$ or ~259 A.

Note that R_{eq} is driven off the size of L1, and if L1 deviates because of manufacturing tolerance, cable inductance, or even EoL battery inductance, then R_{eq} will need to be adjusted. In a manufactured device, R_{eq} should be measured and tuned each time the device is used, but for this study, L1 is chosen as 200 µH, and an R_{eq} of 0.79 was found.

To invert the scaling factor, it is subtracted from the zero-crossing reference r_{zc}—a dimensionless value near unity determined by adding the minimum duty cycle (0.1) to a constant offset of 1. The resulting value is passed through a saturation block to ensure operation remains within the linear region of the power stage. The saturated output then serves as the input to a PWM generator, implemented using the same modulation strategy employed in both Boost Mode and Bypass Mode. This process is shown in Figure 9.

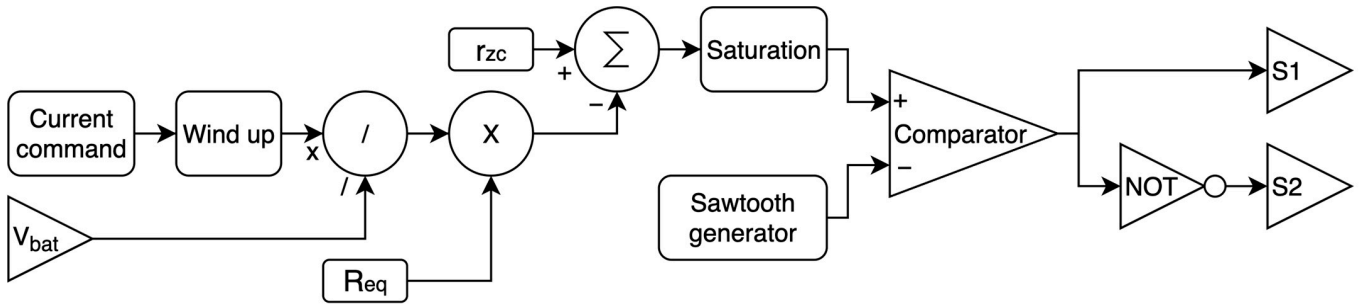

Figure 9. Block diagram of Heating Mode controls with r_{zc} = 1.1 and R_{eq} = 0.79.

3.4. Short-Circuit Mode

Short-Circuit Mode is entered when the EoL battery is at a low enough voltage where, when short-circuited, the current through S2 is low enough for the switch to handle. Since

the current draw is limited by the threshold defined by Heating Mode, the current draw must be limited to 150 A. Assuming the inductor has 10 mΩ, the EoL battery has 10 mΩ, and the switch has 10 mΩ of DC resistance, Short-Circuit Mode can be entered at ~5 V.

4. Simulation Results

Simulation results for all operating modes were generated in PLECS using a common set of model parameters, detailed in Table 2. Thermal analysis of the switches, capacitors, inductors, and the EoL battery are out of the scope of this paper. Figure 10 shows the exact PLECS set up used for all simulations.

Table 2. Key model parameters.

Parameter	Value
L1	200 µH
L1 R_{dc}	10 mΩ
C1/C2	400 µF
C1/C2 ESR	1 mΩ
EoL battery internal resistance	30 mΩ
L2/L3	1 mH
L2/L3 R_{dc}	30 mΩ
S1–S6 R_{ds}	16 mΩ

The EoL battery is modeled as a controllable voltage source with 30 mΩ of internal resistance. The Battery voltage is measured after this internal resistance, meaning that as current is ramped up, the observed battery voltage drops proportionally.

4.1. Bypass Mode

Bypass Mode was validated by sweeping V_{bat} from 1000 V to 400 V, thereby showcasing the system at all expected input voltage ranges. Figure 11 shows that Bypass Mode has <3% THD for all V_{bat} voltages and achieves 50 A_{rms} throughout the sweep when not accounting for state transitions. During Bypass Mode, an average efficiency of 97.9% is measured when considering the switching and conduction losses of all FETs, conductive losses in L1–L3, and conductive losses in C2–C2. Most of the losses occur in L2 and L3.

4.2. Boost Mode

Boost Mode was validated by running two V_{bat} sweeps to showcase starting in Bypass Mode and transitioning to Boost Mode and one sweep starting in Boost Mode. Figure 12 shows the sweep starting in Bypass Mode and validates the state-change process and the entire input operating voltage range. Figure 13 validates starting in Boost Mode and confirms the entire input operating voltage range. Throughout both simulations, DC-bus voltage remains under the 1000 V upper limit and over the 350 V lower limit, with margin to spare. THD also remains under 3%, and the grid current can be maintained at 50 A for the duration of both tests, excluding state transitions.

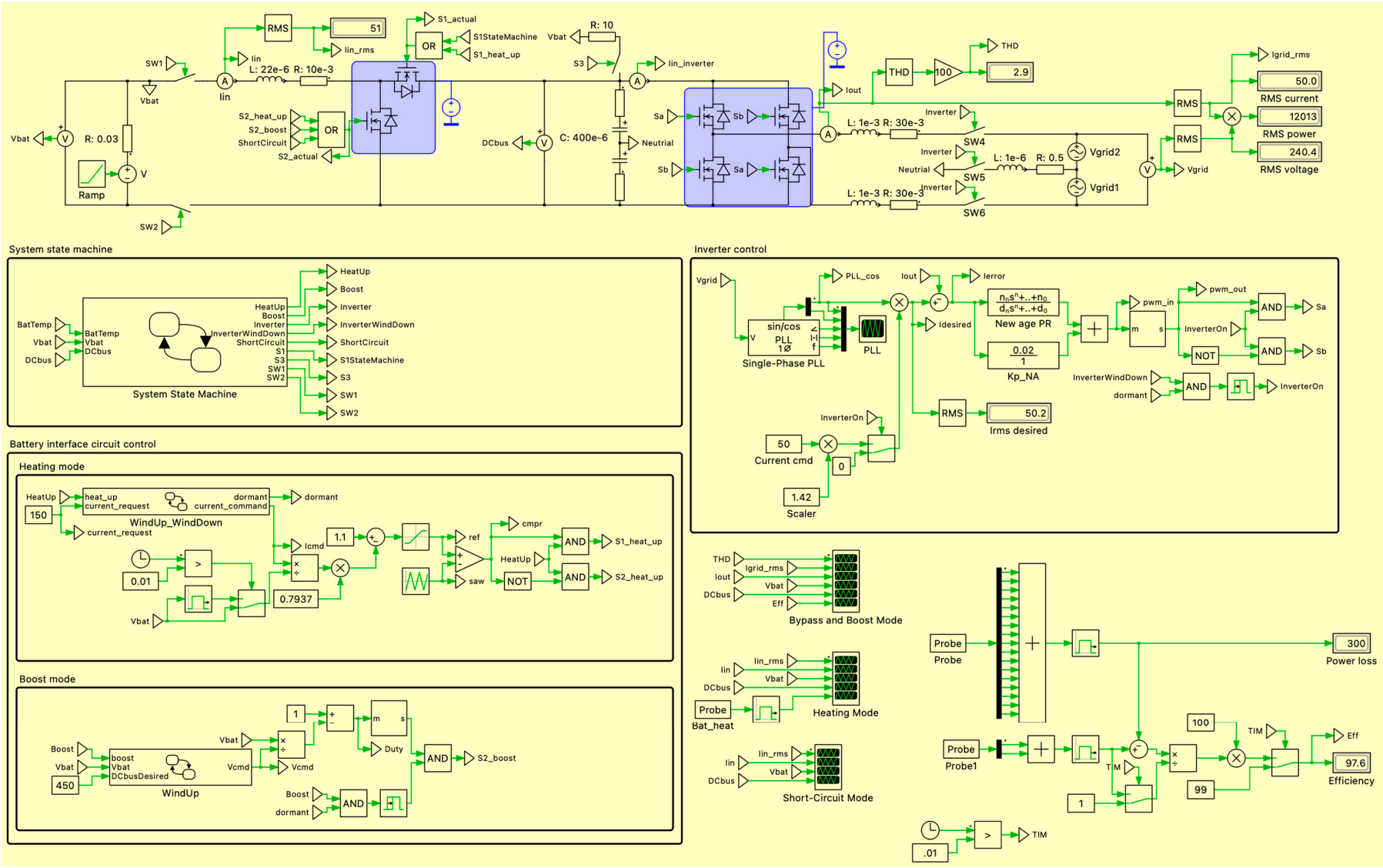

Figure 10. PLECS simulation setup.

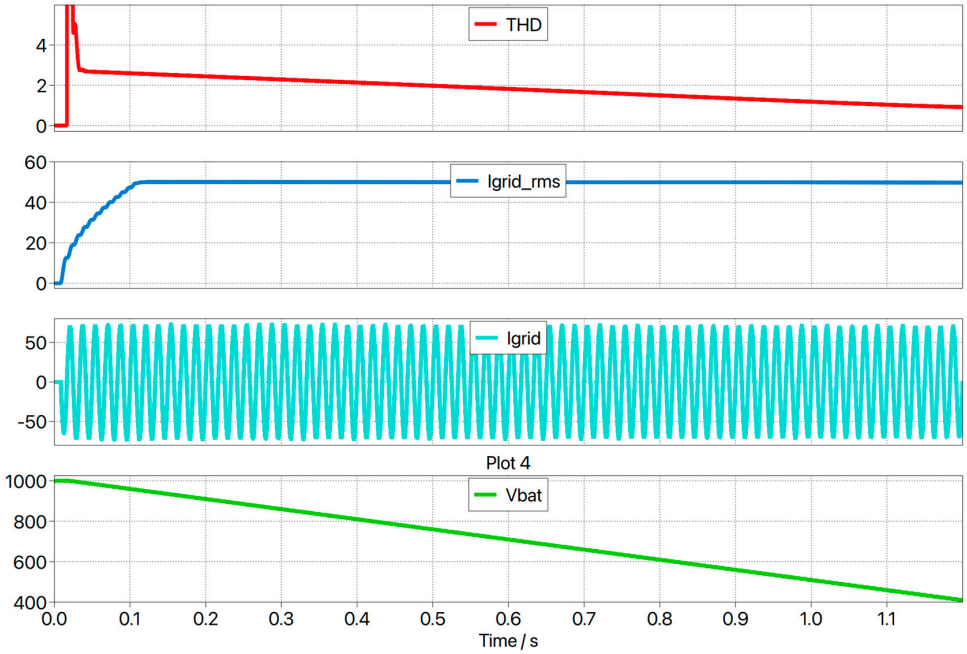

Figure 11. Bypass Mode with V_{bat} sweep from 1000 V to 400 V.

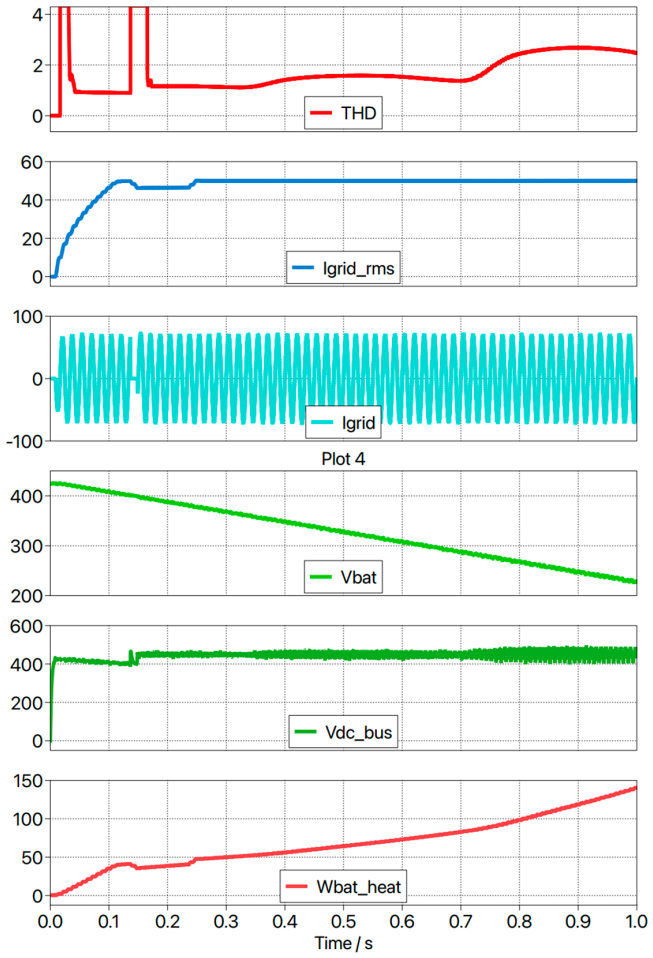

Figure 12. Boost Mode with V_{bat} sweep from 425 V to 200 V.

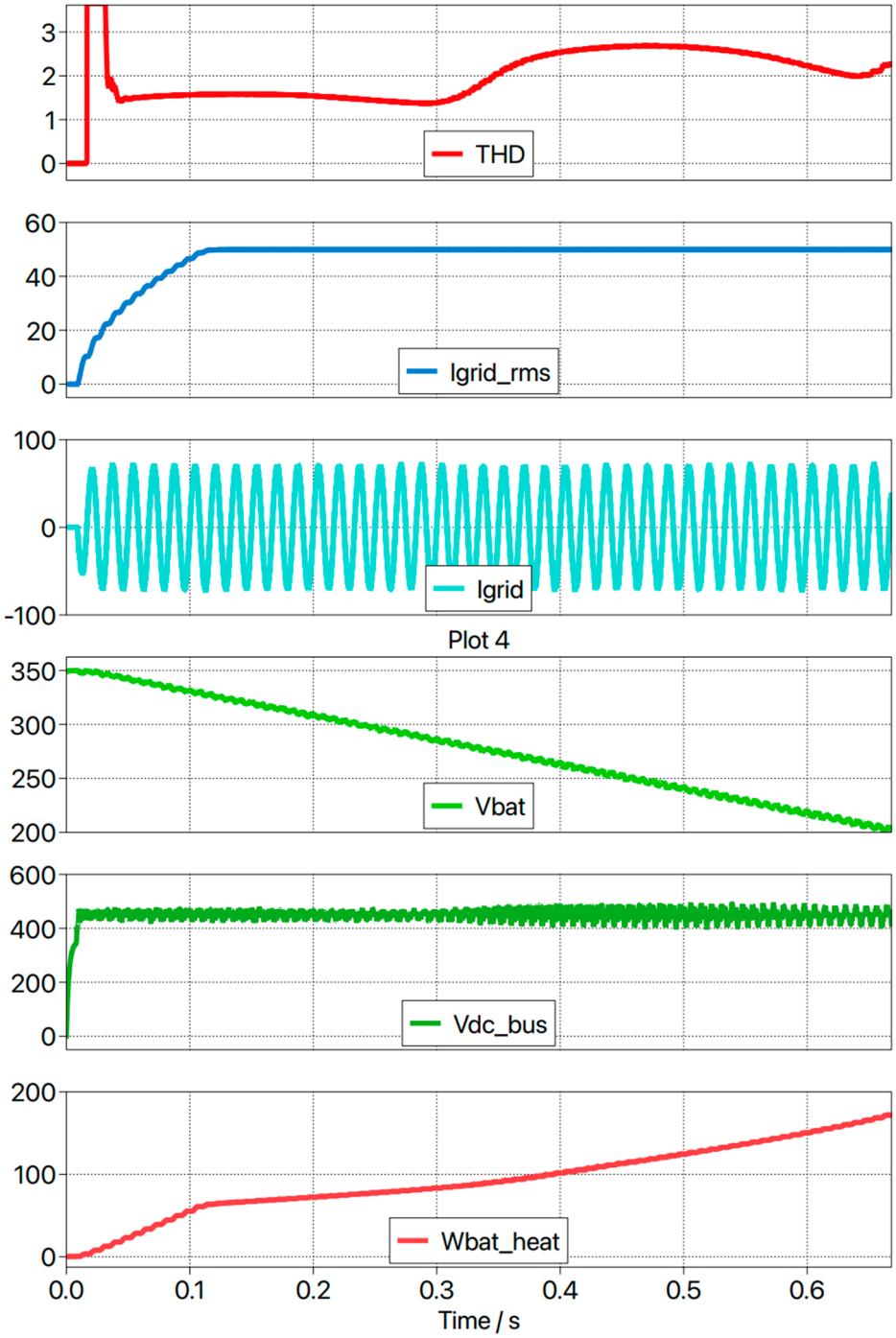

Figure 13. Boost Mode with V_{bat} sweep from 350 V to 200 V.

During Bypass Mode, an average efficiency of 97.5% is measured when considering the switching and conduction losses of all FETs, conductive losses in L1–L3, and conductive losses in C2–C2.

4.3. Heating Mode

Heating Mode was validated by running two V_{bat} sweeps to showcase starting in Boost Mode and transitioning to Heating Mode and one sweep starting in Heating Mode. Figure 14 shows the sweep starting in Heating Mode and validates the state-change process and the entire input operating voltage range. Figure 15 validates starting in Heating Mode and confirms the entire input operating voltage range. Throughout both simulations, DC-bus voltage remains under the 1000 V upper limit. Note that when the EoL battery

voltage drops below around 120 V, the current recirculation circuit is unable to maintain 150 A_{rms} without boosting the DC-bus voltage above the 1000 V limit. At this point, the control system is in saturation and maintains a constant duty cycle.

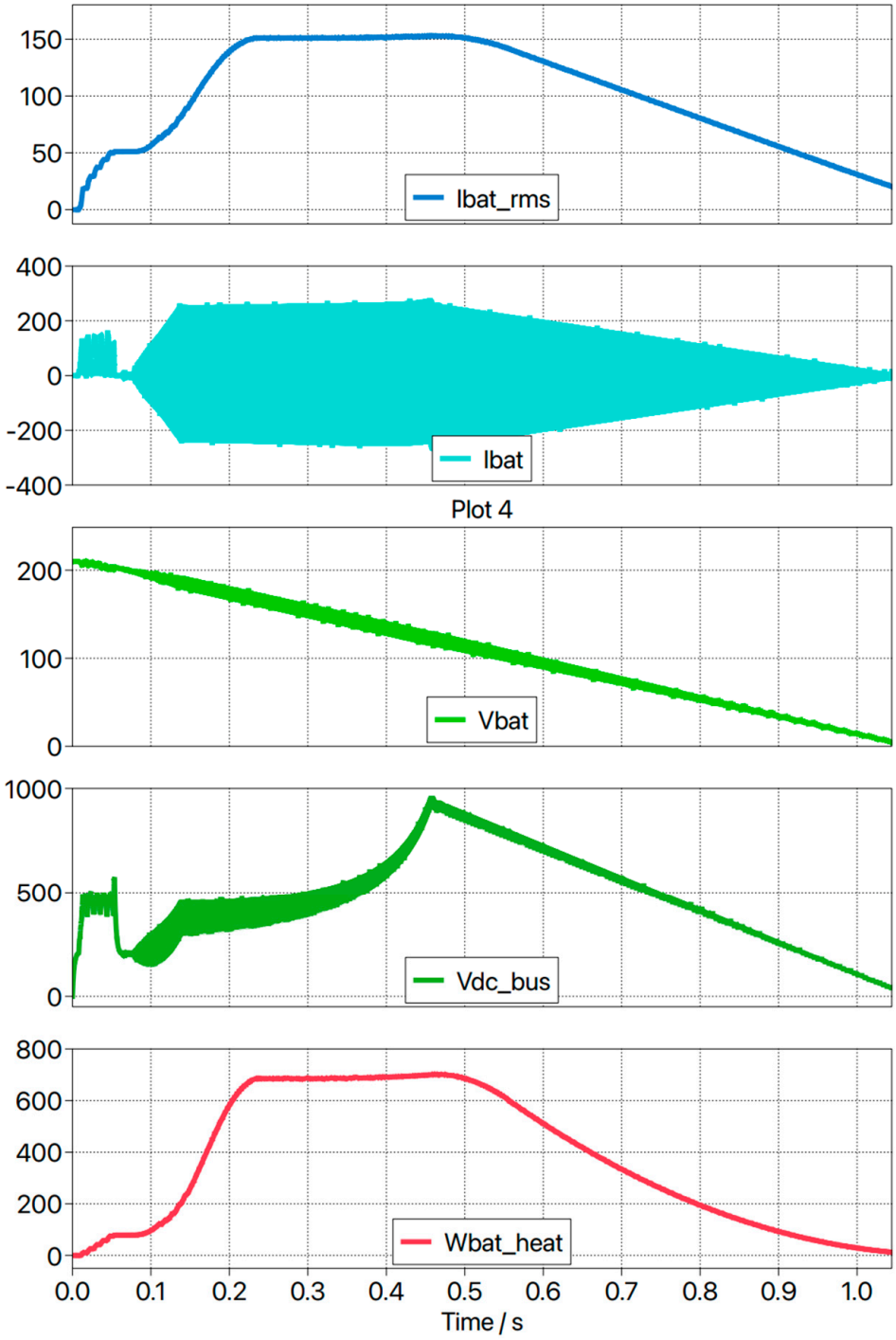

Figure 14. Heating Mode sweeping from 210 V to 5 V.

The heat generated due to conductive losses arising from the internal resistance of the battery, under a sustained current of 150 A_{rms}, is estimated to be 689 W. The thermal capacity of a large-format lithium-ion cell has been reported as 541 J/K for a 489 g cell [21]. Extrapolating this value to a Tesla Model 3 battery pack with an approximate mass of 300 kg yields an estimated total thermal capacitance of 332 kJ/K.

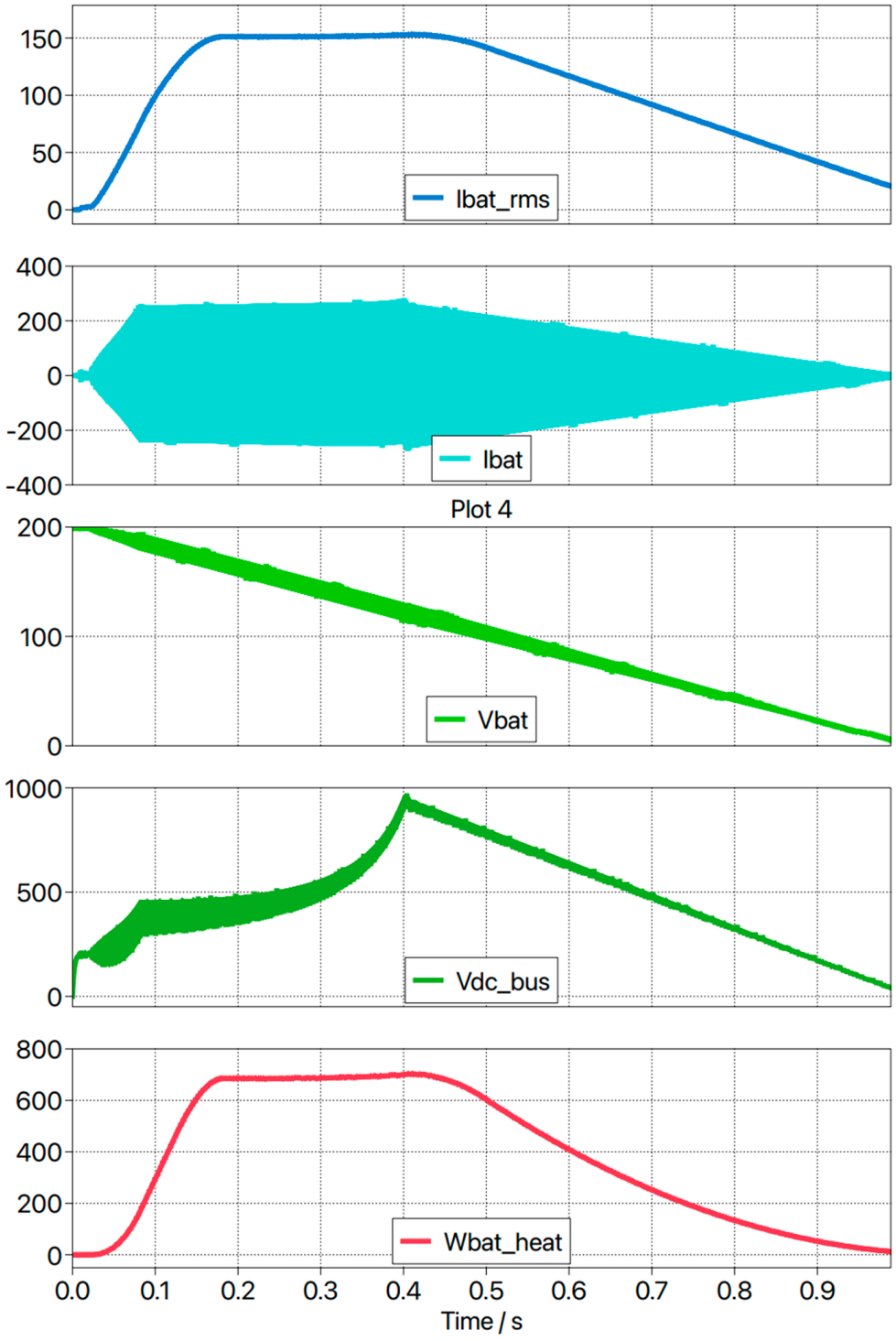

Figure 15. Heating Mode sweeping from 199 V to 5 V.

Assuming a temperature increase from 25 °C to 40 °C, the total thermal energy required is approximately 4.98 MJ (equivalent to 1.38 kWh). During the Bypass and Boost operating modes, the battery is estimated to experience a net heating rate of approximately 100 W. Under the simplifying assumption of negligible thermal losses to the environment, this would result in a temperature increase to approximately 32 °C.

Consequently, an additional energy input of approximately 880 Wh during Heating Mode would be required to reach 40 °C. At an operating current of 150 A_{rms}, this corresponds to a heating duration of approximately 1.3 h. If a battery pack with lower internal resistance is being discharged or if the pack has higher thermal capacity, this time would be

increased. Similarly, if the pack being discharged has higher internal resistance or a lower thermal capacity, this time would be decreased.

Figure 16 shows L1 with a 10% deviation in value without changing the control parameters. Note that V_{dc_bus} increases to 1400 V, which is well above the 1000 V threshold, and the I_{rms} value increases to 185 A_{rms} when prompted for 150 A_{rms}. These deviations in results due to a simple 10% tolerance highlights the need for device parameter tuning during manufacturing.

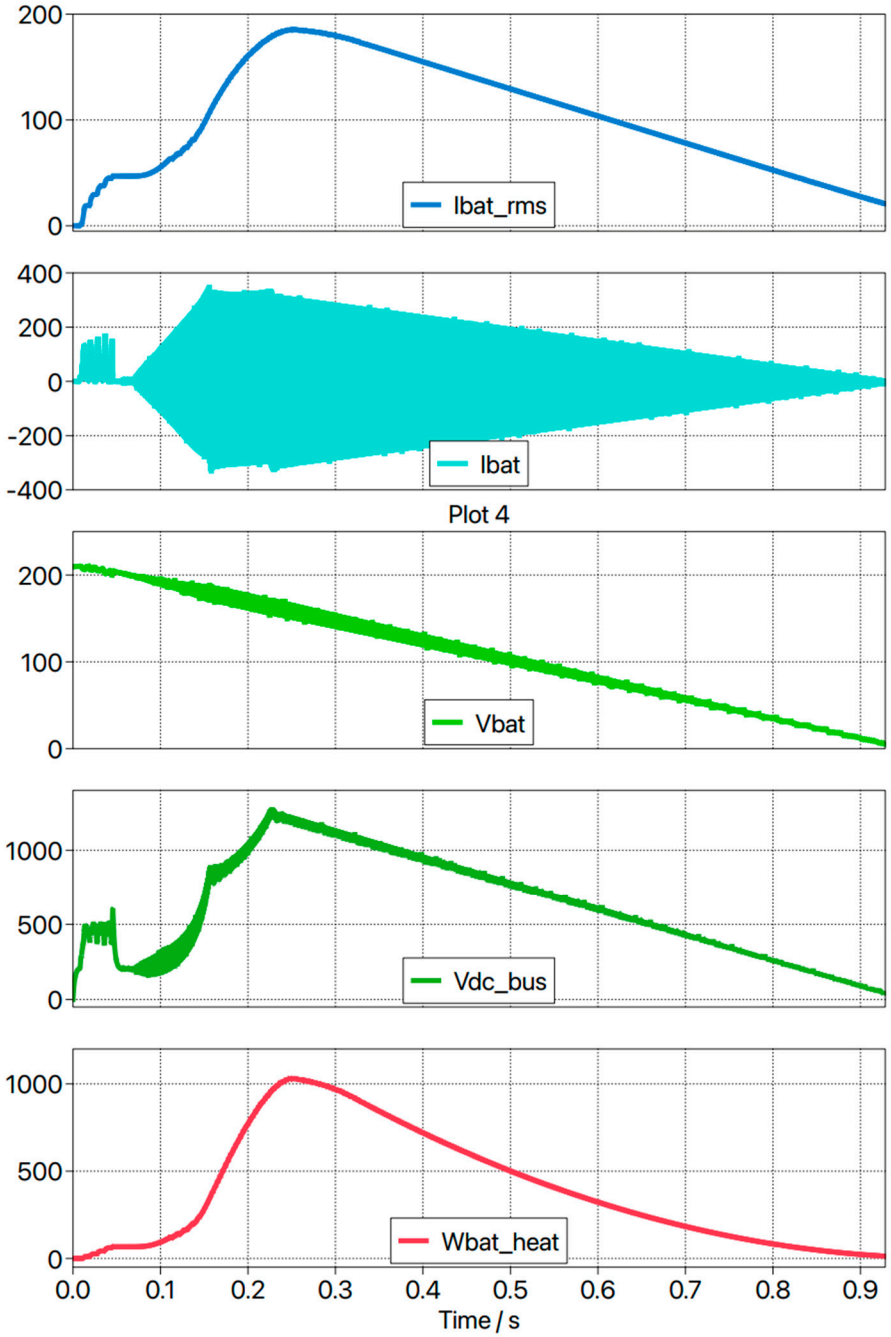

Figure 16. Heating Mode sweeping from 210 V to 5 V with L1 = 220 µH.

4.4. Short-Circuit Mode

Short-Circuit Mode was validated through two V_{bat} sweep simulations: one initiated in Heating Mode and subsequently transitioned into Short-Circuit Mode, and another initialized directly in Short-Circuit Mode. The sweep beginning in Heating Mode, shown in Figure 17, verifies the correctness of the state-transition logic. Figure 18 further demon-

strates proper initialization within Short-Circuit Mode and confirms stable operation across the full intended input voltage range. In both simulations, the EoL battery current remained below the 200A design limit, thereby satisfying the specified safety constraint.

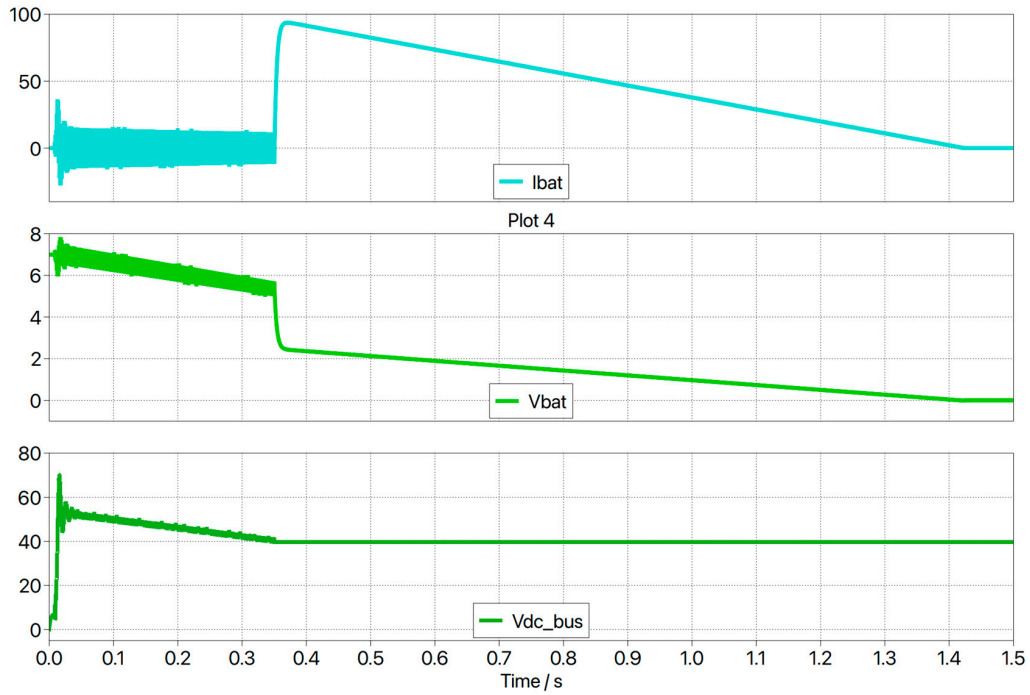

Figure 17. Short-Circuit Mode sweeping from 7 V to 0 V.

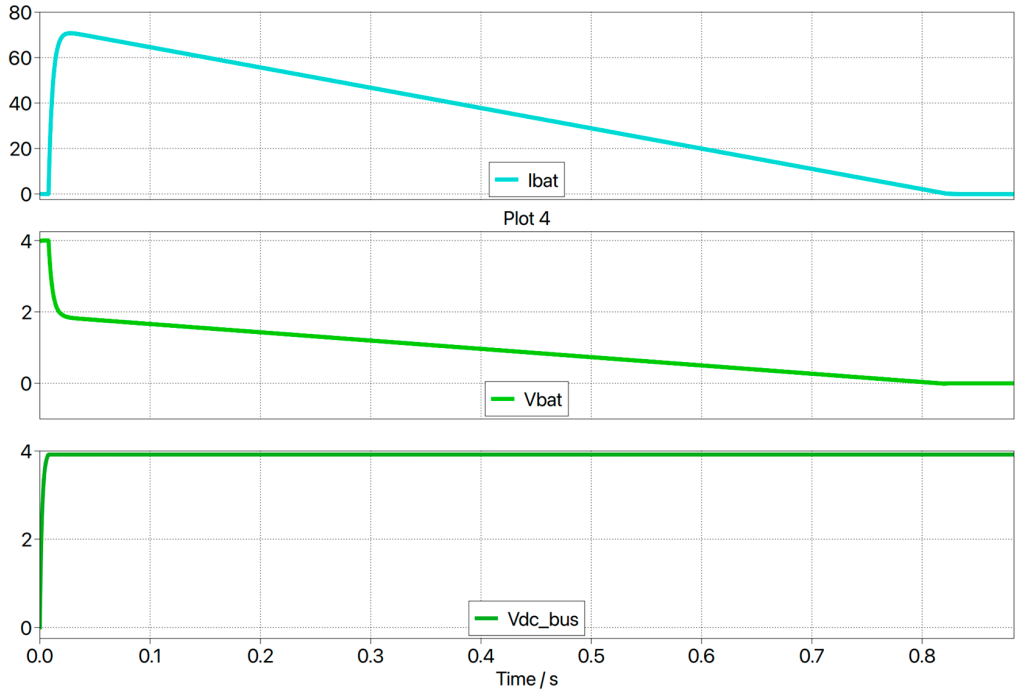

Figure 18. Short-Circuit Mode sweeping from 4 V to 0 V.

The voltage-relaxation behavior of three individual cells measured at different temperatures is shown in the LithoRec study [14]. In the LithoRec study, the cell conditioned at 40 °C exhibited the smallest relaxation [14]. This is consistent with the substantially reduced internal resistance at elevated temperature (reported as ~1.3 mΩ at 40 °C versus ~11.2 mΩ at 0 °C and ~26.5 mΩ at −20 °C shortly after load application) [14]. This temperature dependence aligns with impedance spectroscopy measurements from Western Michigan

University, which show that both interfacial and conductive resistance components decrease markedly as temperature increases (e.g., cathodic interfacial resistance falling multiple-fold when heating from 0 °C to 40 °C, depending on chemistry and SOC) [22]. Maintaining cells at a moderately elevated temperature (around 40 °C) is therefore important because it lowers internal resistance and improves ionic transport, enabling more predictable discharge and relaxation behavior during processing.

In a recycling context, controlling the cells to be 40 °C is safety-relevant: strong temperature-dependent relaxation can lead to significant voltage rebound after disconnecting a short circuit, which may create unexpected electrical hazards in downstream steps (e.g., handling or shredding) if the residual state is misinterpreted.

In addition to temperature, the duration of the applied short circuit is a critical parameter governing subsequent voltage relaxation [14]. To achieve the 5% target described in Section 2, the LithoRec results indicate that a minimum short-circuit period of at least one hour is required, but 24 h is explicitly recommended [14]. However, because processing throughput is a primary economic driver for the proposed device, further investigation is needed to identify the shortest short-circuit duration that still reliably meets the relaxation criterion across relevant cell types and operating conditions. Voltage relaxation typically levels out after 3 or 4 h after the load has been removed [14]. Therefore, it is recommended to check the batteries' voltage relaxation level approximately 5 h after the device has been disconnected from the battery to confirm that it is fully discharged before shredding.

5. Limitations and Future Work

Additional research on energy contained within lithium-ion cells below 2.5 V is also needed to validate acceptable rebound voltage thresholds and to create a model that can be used to simulate the voltage rebound of cells post full discharge. If the amount of energy stored within the battery after voltage rebound is less than that required to heat the thermal capacitance of the battery above 60 °C from room temperature, then shredding should not be able to cause a thermal event.

The present study focused on detailed modeling and simulation, which is a limitation, but the findings indicate a foundation for future hardware development. Verification through hardware, particularly of current recirculation heating effects, grid-tie performance, EMI behavior, and BMS-integrated safety interlocks, will be essential to validate real-world performance.

In regard to safety within a potential hardware design, several additional protective measures must be incorporated. These include an input fuse between L1 and the EoL battery, output fuses on all three grid connection lines, an isolation monitoring device, and switch-level over-temperature and over-current protection. In addition, a dedicated software task with override capability should continuously monitor the EoL pack temperature and disconnect the device if the pack temperature exceeds 45 °C. Columbia University presented a study finding that transformerless EV chargers with V2G capabilities can meet UL standards, which suggests that the topology presented in this paper can achieve practical UL certifications [23].

A further limitation of the present work is that the control architecture was evaluated only in simulation under idealized sensing and actuation assumptions. In a practical prototype, measurement noise in battery voltage, grid voltage, grid current, and pack temperature signals, along with sampling delays, PWM dead time, switch non-idealities, and parameter drift, may alter the observed dynamic response and reduce control accuracy. In particular, the transition boundaries between Bypass, Boost, Heating, and Short-Circuit modes may require hysteresis, filtering, and supervisory timing logic to avoid undesired mode chatter under noisy real-world conditions. Likewise, the open-loop elements used in

the boost and heating controls may prove sensitive to inductance tolerance, cable parasitics, contact resistance, and battery-to-battery variation, indicating that calibration and adaptive parameter identification will likely be necessary in a hardware implementation.

From a real-time implementation perspective, the proposed control structure is feasible with a conventional embedded controller or digital signal processor because the inverter, boost-stage PWM, and mode-transition logic require only standard voltage/current sampling, PLL synchronization, and low-order PR/open-loop duty-cycle calculations. In practice, the PWM and grid-current control loops would operate at the selected 50 kHz switching rate or a synchronized submultiple, while slower supervisory functions—such as BMS temperature monitoring, mode hysteresis, fault checks, and user-interface updates—can run on millisecond-to-second timescales without imposing significant computational burden.

From an implementation standpoint, several practical challenges also remain before the proposed system can be deployed in a workshop or recycling environment. Reliable communication with the battery management system must be established across different manufacturers and pack architectures so that temperature, voltage, and fault data can be acquired with sufficient speed and robustness for safety-critical decisions. In addition, electromagnetic interference, common-mode leakage currents, grounding strategy, enclosure design, thermal management of semiconductor devices and magnetics, and fault handling during abnormal grid or battery conditions must all be experimentally verified. Future work should therefore include the construction of a laboratory prototype and staged validation under realistic operating conditions, including sensor noise, communication interruptions, line disturbances, and component tolerances, to confirm that the proposed topology and control strategy remain safe, stable, and effective outside the simulation environment.

6. Conclusions

This paper introduced a deep-discharge device that integrates a synchronous boost converter, current recirculation heating circuit, and single-phase grid-tied inverter to safely and rapidly process EoL EV batteries. The four-mode operational framework—Bypass, Boost, Heating, and Short-Circuit—enables controlled energy extraction from packs spanning 0–1000 V while also establishing an initial approach for meeting safety requirements, ensuring practical workshop usability, and limiting state-of-charge rebound to below 5%.

Simulations across the full operating range confirmed stable DC-bus behavior, low current distortion, correct state transitions, and proper current limiting, as shown in the mode-validation sweeps (Figures 11–17). These results collectively demonstrate that the proposed architecture can transfer energy efficiently to the grid while also utilizing current recirculation heating to suppress post-discharge voltage recovery. It should be noted that simulation-based results have limitations and experimental results have not been performed.

With this device, discharge times for a Model 3 basic battery pack (57.5 kWh) can be cut down from ~100 h with a brine bath to ~7 h. This difference in time drastically changes the economics of discharge-based EV battery recycling.

A rough estimation of energy consumption, discharge time, total time including labor, voltage relaxation after process, and grid energy recovered for all existing discharge methods is illustrated in Table 3. Note that energy consumption for the proposed system is the efficiency of the system multiplied by the energy in the battery plus the energy required to heat the battery.

Table 3. Quantitative comparison of deep-discharge techniques for Model 3 battery.

Parameter	Proposed System	Existing Inverters	Resistive Load	Brine Bath	Pyrometallurgy
Energy consumption	~3.2 kWh	~2.9 kWh	57.5 kWh	57.5 kWh	57.5 kWh
Discharge time	~7 h	~12 h	~24 h	~100 h	~10 min
Total time including labor	~7.5 h	~22 h	~24.5 h	~101 h	~5 h
Voltage relaxation	~1 V per cell	~1 V per cell	~1 V per cell	0 V per cell	0 V per cell
Grid energy recovered	53.75 kWh	54.6 kWh	0 kWh	0 kWh	0 kWh
Main hazards	BMS comms Link	Exposed HV, Mis-wiring, Short-circuit, Temp sensors misplaced	Fire hazard at high currents, No thermal feedback	Toxic gas, corrosion, casing degradation	Exposed HV, Short-circuit potential

Compared with existing inverters, the proposed system would take ~2.9 times less total time, mainly due to the proposed BMS gateway integration, which eliminates the need for technicians to open the battery, while still recovering similar energy amounts to the power grid. When compared with more common methods like the brine bath, ~18x less energy is consumed in the process while taking ~13.5 times less time to complete a discharge. Only pyrometallurgy beats the proposed system in terms of time, but it has significant downsides such as the remaining need to disassemble the battery before discharge, zero energy returned to the power grid, and the degradation of recyclable materials. Depending on how quickly the batteries can be disassembled, or if a pyrometallurgical process is developed that can ingest entire battery packs, then pyrometallurgy continues to be a strong competitor to our proposed solution. This makes it an attractive option for Redwood Materials.

Nonetheless, the demonstrated control strategy and topology offer the potential for a practical, scalable, and safe pathway for the rapid, standardized deep discharge of EoL EV batteries in service, evaluation, and recycling environments.

7. Patents

A patent application has been submitted for this work and is pending.

Author Contributions: Conceptualization, N.V.K. and C.M.; methodology, E.W.; software, E.W.; validation, E.W.; data curation, E.W.; writing—original draft preparation, E.W.; writing—review and editing, C.M. and N.V.K.; visualization, E.W.; supervision, C.M.; project administration, C.M.; funding acquisition, C.M. All authors have read and agreed to the published version of the manuscript.

Funding: This research was funded by California Energy Commission, grant number EPC-19-053.

Data Availability Statement: The original contributions presented in the study are included in the article, further inquiries can be directed to the corresponding author.

Conflicts of Interest: The authors declare no conflict of interest.

Abbreviations

The following abbreviations are used in this manuscript:

EV	Electric Vehicle
EoL	End-of-Life
SoC	State of Charge
NEMA	National Electrical Manufacturers Association
BMS	Battery Management System
PWM	Pulse-Width Modulation

PLL	Phase-Locked Loop
RMS	Root Mean Squared
PR	Proportional Resonant
THD	Total Harmonic Distortion
DC	Direct Current

References

1. Irle, R. Global EV Sales for 2022, EV-Volumes, 2023. Available online: https://www.ev-volumes.com (accessed on 3 November 2025).
2. Haram, M.H.S.M.; Lee, J.W.; Ramasamy, G.; Ngu, E.E.; Thiagarajah, S.P.; Lee, Y.H. Feasibility of utilising second life EV batteries: Applications, lifespan, economics, environmental impact, assessment, and challenges. *Alex. Eng. J.* **2021**, *60*, 4517–4536. [CrossRef]
3. Munro Live. Inside Redwood Materials: Exclusive Tour & Interview with JB Straubel. *YouTube*. 27 June 2025. Available online: https://www.youtube.com/watch?v=k30syplvCi0 (accessed on 27 June 2025).
4. Biswal, B.K.; Zhang, B.; Tran, P.T.M.; Zhang, J.; Balasubramanian, R. Recycling of spent lithium-ion batteries for a sustainable future: Recent advancements. *Chem. Soc. Rev.* **2024**, *53*, 5552–5592. [CrossRef] [PubMed]
5. Cornelio, A.; Zanoletti, A.; Bontempi, E. Recent progress in pyrometallurgy for the recovery of spent lithium-ion batteries: A review of state-of-the-art developments. *Curr. Opin. Green Sustain. Chem.* **2024**, *46*, 100881. [CrossRef]
6. Lee, J.; Park, K.W.; Sohn, I.; Lee, S. Pyrometallurgical recycling of end-of-life lithium-ion batteries. *Int. J. Miner. Metall. Mater.* **2024**, *31*, 1554. [CrossRef]
7. Beaudet, A.; Larouche, F.; Amouzegar, K.; Bouchard, P.; Zaghib, K. Key challenges and opportunities for recycling electric vehicle battery materials. *Sustainability* **2020**, *12*, 5837. [CrossRef]
8. Nakoul, S.M. Hydrometallurgy: Principles, processes and applications. *J. Powder Metall. Min.* **2024**, *13*, 1000433. Available online: https://www.omicsonline.org/open-access-pdfs/hydrometallurgy-principles-processes-and-applications.pdf (accessed on 27 June 2025).
9. Dias, M.E.D.M.G.; Tenório, J.A.S.; Espinosa, D.C.R.; Botelho Junior, A.B. Recycling of Li-ion batteries: Recovery of critical metals by hydrometallurgy. *JOM* **2026**, *78*, 1188–1199. [CrossRef]
10. Cheng, K.; Crumbley, D.L. Canada's Li-Cycle Holdings Corporation: Innovative Technology and Innovative Accounting for Off-Take Agreements. *J. Forensic Investig. Account.* **2023**, *15*, 261–271.
11. Xiao, J.; Jiang, C.; Wang, B. A Review on Dynamic Recycling of Electric Vehicle Battery: Disassembly and Echelon Utilization. *Batteries* **2023**, *9*, 57. [CrossRef]
12. Garg, N.; Pekkinen, S.; González, E.M.; Serna-Guerrero, R.; Peljo, P.; Santasalo-Aarnio, A. Enhanced electrochemical discharge of Li-ion batteries for safe recycling. *Sustain. Energy Fuels* **2024**, *8*, 2777–2788. [CrossRef] [PubMed]
13. DV Power. Battery Load Unit BLU-A. Available online: https://www.dv-power.com/product/battery-capacity-testers/battery-load-unit-blua/ (accessed on 6 April 2026).
14. Kwade, A.; Diekmann, J. (Eds.) *Recycling of Lithium-Ion Batteries: The LithoRec Way*; Springer International Publishing: Cham, Switzerland, 2018. [CrossRef]
15. Mi, C.C.; Gao, W. Flexible Battery Management System (BMS)-Gateways and Modular Energy Management Systems for Second-Life Electric Vehicle (EV) Batteries in Energy Storage Systems. U.S. Patent Application No. US 2025/0118982 A1, 10 April 2025.
16. Hart, D.W. *Power Electronics*; McGraw-Hill: New York, NY, USA, 2011.
17. Chen, M.; Rincón-Mora, G.A. Accurate electrical battery model capable of predicting runtime and I–V performance. *IEEE Trans. Energy Convers.* **2006**, *21*, 504–511. [CrossRef]
18. Kamalini, C.P.; Suganyadevi, M.V.; Freetha, B.; Shree, M. Design and implementation of proportional resonant controller for power inverters. *Int. J. Eng. Res. Appl.* **2021**, *11*, 25–31. [CrossRef]
19. Nowak, M.; Binkowski, T.; Piróg, S. Proportional–resonant controller structure with finite gain for three-phase grid-tied converters. *Energies* **2021**, *14*, 6726. [CrossRef]
20. Mohan, N. *Power Electronics: A First Course*; John Wiley & Sons: Hoboken, NJ, USA, 2012.
21. Lin, J.; Chu, H.N.; Monroe, C.W.; Howey, D.A. Anisotropic thermal characterisation of large-format lithium-ion pouch cells. *arXiv* **2021**, arXiv:2112.09768. [CrossRef]

22. Ahmed, S.H.; Kang, X.; Shrestha, S.O.B. Effects of temperature on internal resistances of lithium-ion batteries. *J. Energy Resour. Technol.* **2015**, *137*, 031901. [CrossRef]
23. Jahnes, M.; Zhou, L.; Eull, M.; Wang, W.; Preindl, M. Design of a 22 kW transformerless EV charger with V2G capabilities and peak 99.5% efficiency. *IEEE Trans. Ind. Electron.* **2022**, *70*, 5862–5871. [CrossRef]